

Reconciling *Planck* cluster counts and cosmology? *Chandra/XMM* instrumental calibration and hydrostatic mass bias

Holger Israel,¹★ Gerrit Schellenberger,² Jukka Nevalainen,³ Richard Massey¹ and Thomas H. Reiprich²

¹*Institute for Computational Cosmology, Department of Physics, Durham University, South Road, Durham DH1 3LE, UK*

²*Argelander-Institut für Astronomie, Auf dem Hügel 71, D-53121 Bonn, Germany*

³*Tartu Observatory, 61602 Toravere, Estonia*

Accepted 2015 January 7. Received 2014 November 28; in original form 2014 August 20

ABSTRACT

The mass of galaxy clusters can be inferred from the temperature of their X-ray-emitting gas, T_X . Their masses may be underestimated if it is assumed that the gas is in hydrostatic equilibrium, by an amount $b^{\text{hyd}} \sim (20 \pm 10)$ per cent suggested by simulations. We have previously found consistency between a sample of observed *Chandra* X-ray masses and independent weak lensing measurements. Unfortunately, uncertainties in the instrumental calibration of *Chandra* and *XMM-Newton* observatories mean that they measure different temperatures for the same gas. In this paper, we translate that relative instrumental bias into mass bias, and infer that *XMM-Newton* masses of $\sim 10^{14} M_\odot$ ($\gtrsim 5 \times 10^{14} M_\odot$) clusters are unbiased (~ 35 per cent lower) compared to weak lensing masses. For massive clusters, *Chandra*'s calibration may thus be more accurate. The opposite appears to be true at the low-mass end. We observe the mass bias to increase with cluster mass, but presence of Eddington bias precludes firm conclusions at this stage. Nevertheless, the systematic *Chandra* – *XMM-Newton* difference is important because *Planck*'s detections of massive clusters via the Sunyaev–Zeldovich (SZ) effect are calibrated via *XMM-Newton* observations. The number of detected SZ clusters are inconsistent with *Planck*'s cosmological measurements of the primary cosmic microwave background. Given the *Planck* cluster masses, if an (unlikely) uncorrected ~ 20 per cent calibration bias existed, this tension would be eased, but not resolved.

Key words: gravitational lensing weak – galaxies: clusters: general – cosmology: observations – X-rays: galaxies: clusters.

1 INTRODUCTION

The number of Sunyaev–Zeldovich (SZ) clusters detected with *Planck* above a certain mass threshold (Planck Collaboration XX 2014, hereafter P13XX) falls short of the tally expected from the *Planck* primary cosmic microwave background (CMB) constraints on cosmology (Planck Collaboration XVI 2014, hereafter P13XVI). Several possible explanations have been brought forward, such as incorrect assumptions about the cluster mass function (P13XX) or modified cosmologies including massive neutrinos and a shift in the Hubble parameter (Hamann & Hasenkamp 2013; Battye & Moss 2014; Costanzi et al. 2014; Mantz et al. 2014; P13XX). Another hypothesis is that hydrostatic cluster masses, inferred from X-ray observations of the intracluster medium (ICM), yielded only ~ 60 per cent of the true cluster mass. Hydrodynamic cluster simulations commonly find the hydrostatic assumption

to retrieve only ~ 70 – 90 per cent of the true cluster mass, i.e. $M^{\text{HE}} = (1 - b_{\text{lin}}^{\text{hyd}})M^{\text{true}}$ with a hydrostatic mass bias $b_{\text{lin}}^{\text{hyd}} = 0.1$ – 0.3 (e.g. Nagai, Kravtsov & Vikhlinin 2007; Laganá, de Souza & Keller 2010; Kay et al. 2012; Rasia et al. 2012; Le Brun et al. 2014; Schaye et al. 2014).

The validity of the assumption of hydrostatic equilibrium can potentially be addressed by comparing to weak gravitational lensing (WL) mass measurements, which are independent and free from assumptions of the state of the gas. Noticing a considerable overlap between the *XMM-Newton* sample of P13XX and the *Weighing the Giants* WL survey (Applegate et al. 2014; Kelly et al. 2014; von der Linden et al. 2014a), von der Linden et al. (2014b, hereafter vdL14) measured $\langle M^{\text{pl}}/M^{\text{wl}} \rangle = 0.688 \pm 0.072$ for the most massive ($> 6 \times 10^{14} M_\odot$) clusters. If interpreted as a hydrostatic mass bias, this value $b_{\text{lin}} \approx 0.3$ falls short of the $b_{\text{lin}} \approx 0.4$ necessary to reconcile P13XX with P13XVI, confirming the *Planck* cluster mass discrepancy.

Conversely, Israel et al. (2014, hereafter I14) found no significant mass bias when comparing WL estimates to *Chandra*-based

* E-mail: holger.israel@durham.ac.uk

hydrostatic masses. For high-mass clusters ($10^{14.5} M_{\odot} < M_{500}^{\text{wl}} < 10^{15} M_{\odot}$), the bias $b_{\log} = -0.10_{-0.15}^{+0.17}$, is consistent with the expectation based on simulations, although with large uncertainties due to small number statistics.

An alternative hypothesis is that at least one of the two X-ray observatories is imperfectly calibrated. Indeed, difficulties modelling their (energy-dependent) effective collecting area (Grant et al. 2013) lead to uncertainty in measurements of the ICM temperature, T_X . Direct comparisons have shown that *Chandra* measures significantly higher T_X than *XMM-Newton* for the same clusters (e.g. Nevalainen, David & Guainazzi 2010), and that significant differences even exist between the *XMM-Newton* instruments (Schellenberger et al. 2014, hereafter S14). S14 propagated this difference to a change in the inferred cosmological matter density Ω_m and power-spectrum normalization σ_8 . They concluded that the temperature calibration alone is insufficient to explain the discrepancy between P13XVI and P13XX.

In this paper, we simultaneously examine the hydrostatic bias and *XMM-Newton/Chandra* instrument calibration, aiming to find a solution for the cosmological discrepancy. We extend S14 by comparing measurements in an X-ray-selected cluster sample with independent WL masses. In Section 2, we re-evaluate I14's measurements of the mass bias between *Chandra* hydrostatic and WL masses, and emulate *XMM-Newton* results based on S14's cross-calibration. Noting that the P13XX calibration relies on *XMM-Newton*, in Section 3, we assess the degree to which X-ray temperature calibration could be responsible for the P13XVI–P13XX discrepancy. We conclude in Section 4.

2 RECALIBRATING THE 400d SURVEY TO XMM-NEWTON TEMPERATURES

2.1 Hydrostatic mass bias from the 400d cluster cosmology survey

I14 recently compared WL masses to *Chandra*-based X-ray mass estimates for eight clusters drawn from the 400d cosmology cluster sample. The 400d cosmology sample selects X-ray luminous clusters at $0.35 < z < 0.90$ from the serendipitous 400d *Rosat* cluster catalogue (Burenin et al. 2007). *Chandra* data for these clusters were subsequently employed to constrain cosmological parameters via the cluster mass function (Vikhlinin et al. 2009a,b, hereafter V09a,b). The 400d WL survey follows up the cosmology cluster sample, in order to test the mass calibration of V09a,b with independent mass estimates. The methodology and first results of the ongoing 400d WL survey were reported in Israel et al. (2010, 2012). We refer the interested reader to these papers for details. Weak lensing masses used in this paper make use of the Bhattacharya et al. (2013) mass–concentration relation.

Hydrostatic masses in I14 were derived from the V09a *Chandra* ICM density profiles ρ_g using the Vikhlinin et al. (2006) parametrization, and temperatures $T_X(r) = T_{\text{CXO}}(r)$. The empirical Reiprich et al. (2013) relation was used to derive a temperature profile

$$T_X(r) = T_X (1.19 - 0.84r/r_{200}) \quad (1)$$

from a cluster-averaged value T_X and I14 WL radius r_{200} . This relation was determined and can be used in the range $0.3 r_{200} < r < 1.15 r_{200}$. We then compute

$$M^{\text{HE}}(r) = \frac{-k_B T_X(r) r}{\mu m_p G} \left(\frac{d \ln \rho_g(r)}{d \ln r} + \frac{d \ln T_X(r)}{d \ln r} \right), \quad (2)$$

with k_B the Boltzmann constant, $\mu = 0.5954$ the mean molecular mass of the ICM, m_p the proton mass, and G the gravitational constant. The resulting cumulative mass profile was evaluated at r_{500} taken from WL. Uncertainties on T_{CXO} and r_{500}^{wl} were propagated into an uncertainty on $M_{500}^{\text{hyd}}(r_{500}^{\text{wl}})$.

2.2 Monte Carlo analysis

We adopt a Monte Carlo approach to derive hydrostatic masses. In our scheme, the V09a cluster-averaged temperature T_{CXO} , the square of the Israel et al. (2012, hereafter I12) WL cluster radius $(r_{500}^{\text{wl}})^2$, and the slope, normalization, and intrinsic scatter of the S14 *Chandra* – *XMM-Newton* calibration relation are sampled from their Gaussian distributed probability densities. We point out that we model each of our clusters independently. By choosing $(r_{500}^{\text{wl}})^2$, whose I12 measurements we empirically find to follow a normal distribution, we are able to easily reproduce the asymmetric uncertainties in r_{500} , improving our treatment from I14. Using 10^6 Monte Carlo realizations, we excellently recover the I12 WL masses. Through the use of r_{500}^{wl} in equation (1), the updated account of its asymmetric uncertainties results in slightly lower *Chandra* hydrostatic masses. Compared to I14, *Chandra* hydrostatic masses are lower by an average (1.2 ± 0.3) per cent (compare tables 1 to 2 of I14). Our new Monte Carlo technique leads to smaller uncertainties in the hydrostatic masses compared to the conservative combination of uncertainties in T_{CXO} and r_{500}^{wl} that was employed by I14.

2.3 Pseudo-XMM-Newton temperatures for the 400d clusters

The International Astronomical Consortium for High Energy Calibration has tasked itself with improving (cross-)calibrations of X-ray satellite observatories (Grant et al. 2013). In this context, S14 published a detailed comparison of *Chandra* and *XMM-Newton* temperatures for the Hightes X-ray FLUX Galaxy Cluster sample (HIFLUGCS; Reiprich & Böhringer 2002) of 64 high-flux local clusters, fitting spectra in the same radial and energy ranges. They not only confirmed earlier studies (e.g. Nevalainen et al. 2010) that *Chandra* yields significantly higher T_X than *XMM-Newton*, but also find significant differences between the *XMM-Newton* instruments. These temperature differences are most pronounced at the highest plasma temperatures and can best be explained as calibration uncertainties on effective area.

For the 400d cluster sample, we translate ICM temperatures measured with *Chandra*, T_{CXO} , to pseudo-*XMM-Newton* temperatures by applying the S14 conversion formula between Advanced CCD Imaging Spectrometer (ACIS) and the combined *XMM-Newton* instruments for 0.7–7 keV energy range:

$$\log \left(\frac{k_B T_{\text{XMM}}}{1 \text{ keV}} \right) = A \times \log \left(\frac{k_B T_{\text{CXO}}}{1 \text{ keV}} \right) + B. \quad (3)$$

Both the calibration of an X-ray instrument and our knowledge about it evolve with time. S14 assume calibrations as of 2012 December (*Chandra* Calibration Database v4.2), while V09a used the unchanged Vikhlinin et al. (2005) calibration procedure. This is no Calibration Database calibration, but at the time of observation v3.1 was in place. Therefore, we apply the following steps to derive pseudo-*XMM-Newton* temperature profiles.

(1) We transform the V09a T_{CXO} from the energy range of 0.6–10 to 0.7–7 keV, by applying a correction

$$\log \left(\frac{k_B T_{\text{CXO}}^{(0.7-7)}}{1 \text{ keV}} \right) = A_0 \times \log \left(\frac{k_B T_{\text{CXO}}^{(0.6-10)}}{1 \text{ keV}} \right) + B_0 \quad (4)$$

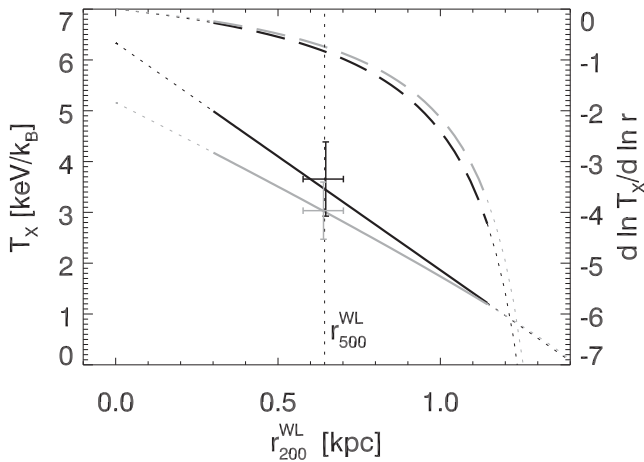


Figure 1. The effect of re-calibration on the temperature profile. The black solid line shows the Reiprich et al. (2013) *Chandra* temperature profile we assume for CL 0030+2618. By applying equation (3), which is linear in $\log T_X$, to each datum of the profile, we derive the grey solid pseudo-*XMM-Newton* profile, which is slightly curved, but still close to the Reiprich et al. (2013) form. As indicated by the vertical line, r_{500} lies safely within the range (bold lines) in which the Reiprich et al. (2013) profile can be used. Long-dashed curves denote the logarithmic derivatives. For the sake of clarity, uncertainties are only shown at r_{500} .

with $A_0 = 1.0027 \pm 0.0018$ and $B_0 = -0.0008 \pm 0.0013$ derived from fitting the *Chandra* temperatures of the HIFLUGCS sample in the two spectral ranges, in analogy to S14. This raises the T_{CXO} values by 0.1–0.3 per cent.

(2) Using the timestamp correction for T_X between different Calibration Databases (Reese et al. 2010), derived for the 0.7–7 keV band, we convert the V09a temperatures to the one used by S14 (version 4.2). From equation 23 of Reese et al. (2010), we take a factor of $T_{CXO, 3.1}/T_{CXO, 4.2} = 1.06 \pm 0.05$.

(3) For each of the 10^6 Monte Carlo realizations, we compute the *Chandra* temperature profile following equation (1). The black solid line in Fig. 1 shows an example (CL 0030+2618).

(4) Finally, we perform the transformation (equation 3) between *Chandra* and the combined *XMM-Newton* instruments, in the 0.7–7 keV energy range. The best-fitting parameters taken from S14 are $A = 0.889^{+0.005}_{-0.003}$ and $B = 0.000 \pm 0.004$. This transformation is applied to every datum of the temperature profile. As the grey solid line in Fig. 1 shows, the re-calibration introduces a slight curvature, because equation (3) is linear in $\log T_X$ rather than in T_X . Given the measurement uncertainties, the resulting departure from the form of equation (1) is insignificant.

By applying this conversion, we emulate what ICM temperatures would have been obtained for the 400d clusters, had they been inferred from both the Metal Oxide Semi-conductor (MOS) and the pn-CCD (PN) instruments (collectively, the *XMM-Newton* European Photon Imaging Camera, EPIC) instead of *Chandra*'s ACIS. We denote the resulting temperatures T_{xmm} , with the lowercase indicating that they are converted quantities, not actual *XMM-Newton* measurements.

For the eight I14 clusters, whose $\langle T_{CXO} \rangle = 4.4$ keV/ k_B is representative of the full 400d cosmology sample, we measure $\langle T_{xmm}/T_{CXO} \rangle = 0.81 \pm 0.01$, using the V09a cluster-averaged temperatures. At r_{500} , measured from weak lensing, the ratio is $\langle T_{xmm}/T_{CXO} \rangle = 0.85 \pm 0.01$. This ratio is closer to 1 because

$T_X(r_{500}) < \langle T_X \rangle$ and the cross-calibration differences are smaller for lower T_X according to S14.

2.4 Pseudo-*XMM-Newton* hydrostatic masses

Within our Monte Carlo scheme, we re-derive hydrostatic masses by inserting the pseudo-*XMM-Newton* profiles $T_{xmm}(r)$ and their values at r_{500} into equation (2), thus accounting for the non-linear nature of equation (3).

Differences in the effective area normalization between *Chandra* and *XMM-Newton* also affect the measured gas mass M_{gas} and hydrostatic mass via the calibration of the flux S . As $M_{gas} \propto \sqrt{S}$, the 5 per cent flux difference for the full energy range in Nevalainen et al. (2010) corresponds to 2 per cent uncertainty in M_{gas} . We account for this effect by rescaling the pseudo-*XMM-Newton* masses by 0.98.

As expected for lower input temperatures and flatter T_X gradients, we find the resulting pseudo-*XMM-Newton* hydrostatic masses for all clusters to be lower than the *Chandra*-measured values (Fig. 2). We point out that in Fig. 2, we do not apply the timestamp correction to the T_{CXO} , to highlight the combined effect of both corrections. The relative difference in masses is strongest for the hottest clusters, for which the S14 conversion results in the largest change. Because the I14 sample exhibits a limited T_X range of 3–6 keV, the relative change of the temperatures varies less than 5 per cent. Consequently, the two sets of hydrostatic masses are well fit by a linear relation (solid line in Fig. 2):

$$\frac{M_{500}^{xmm}}{10^{14} M_{\odot}} = P \times \frac{M_{500}^{CXO}}{10^{14} M_{\odot}} + Q \quad (5)$$

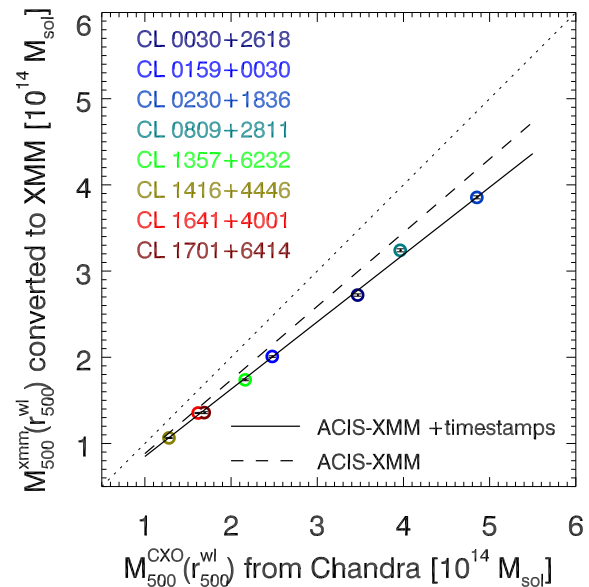


Figure 2. Mass estimates M_{500}^{xmm} derived from pseudo-*XMM-Newton* temperatures and assuming hydrostatic equilibrium as a function of masses M_{500}^{CXO} derived from ICM temperatures observed by *Chandra*. Error bars inscribed in the symbols denote the uncertainty in M_{500}^{xmm} due to the uncertainties in the ACIS-combined *XMM* and timestamp conversions. For illustrative purposes, the timestamp correction is not applied to the M_{500}^{CXO} , but its inverse to the M_{500}^{xmm} . The solid line marks the linear best fit. A dashed line marks the best-fitting relation when the different *Chandra* calibration timestamps are not taken into account. For the latter case, data points are not shown for the sake of clarity.

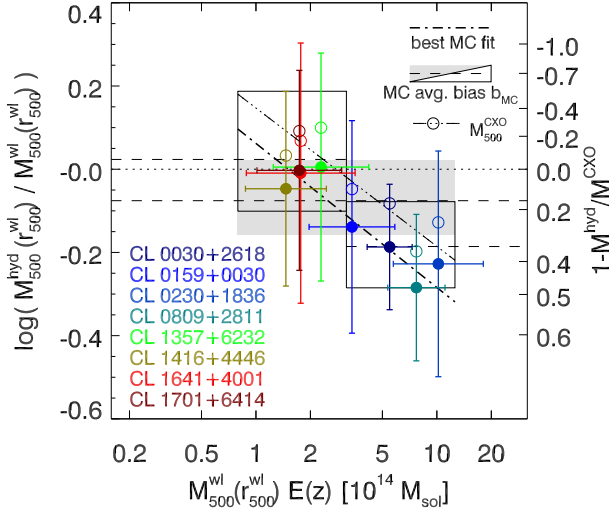


Figure 3. Ratio between the pseudo-*XMM-Newton* hydrostatic mass M_{500}^{xmm} , with timestamp correction, and the I14 WL mass M_{500}^{wl} as a function of M_{500}^{wl} . Short-dashed lines and light grey shading denote the logarithmic bias $b_{\log} = \langle \log M^{\text{xmm}} - \log M^{\text{wl}} \rangle$ obtained from averaging over Monte Carlo realizations. We also show b_{\log} for the low- and high- M^{wl} clusters separately, with the 1σ uncertainties presented as boxes, for sake of clarity. As a visual aid, a dot-dashed line depicts the Monte Carlo best fit of $\log(M^{\text{xmm}}/M^{\text{wl}})$ as a function of M^{wl} . Empty symbols and the triple-dot-dashed line denote the M_{500}^{CXC} case. Compare to fig. 2A in I14.

with $P = 0.783 \pm 0.007$ and $Q = 0.062 \pm 0.015$ that captures the dependence of the *Chandra-XMM-Newton* disagreement on the measured mass itself. As a sample average and standard error, we find $1 - b_{\text{lin}}^{\text{cal}} = 1 - \langle M_{500}^{\text{xmm}}/M_{500}^{\text{CXC}} \rangle = 0.81 \pm 0.01$. The difference between this number and $1 - \langle T_{\text{xmm}}(r_{500}^{\text{wl}})/T_{\text{CXC}}(r_{500}^{\text{wl}}) \rangle = 0.15 \pm 0.01$ can be traced back to the additional factor of T_X ($\frac{d \ln T_X(r)}{d \ln r}$) in equation (2).

2.5 Stronger WL mass bias for pseudo-*XMM-Newton* masses

Fig. 3 shows the measured bias between the WL masses M_{500}^{wl} and M_{500}^{xmm} (including timestamp correction) for the I14 clusters. The bias is measured by averaging $\langle \log M^{\text{xmm}} - \log M^{\text{wl}} \rangle$ over the suite of Monte Carlo simulations described in Section 2.2 that was used to obtain the M_{500}^{xmm} measurements. The results are shown in Table 1 and indicated by a dashed line and shading for the 1σ interval in Fig. 3. Dashed lines and boxes at $M_{500}^{\text{wl}} \leq 10^{14.5} M_{\odot}$ and $M_{500}^{\text{wl}} \geq 10^{14.5} M_{\odot}$ show the bias for the thus-defined low- and high-mass sub-samples.

Table 1. Observed mass bias in the I14 sample, for several choices of X-ray masses. Columns 2 and 3 give the slope P and intercept Q of the general best-fitting relation (equation 5) between *Chandra* and *XMM-Newton* masses. Column 4 shows the X-ray calibration bias, i.e. the mean and standard error of $\langle M_{500}^{\text{xmm}}/M_{500}^{\text{CXC}, \text{I14}} \rangle$. Columns 5 and 6 show the apparent bias with respect to the WL masses, averaged over Monte Carlo simulations for all clusters ($b_{\log} = \langle \log M_{500}^{\text{xmm}} - \log M_{500}^{\text{wl}} \rangle$) and for the $M_{500}^{\text{wl}} \geq 10^{14.5} M_{\odot}$ bin ($b_{\log, \text{H}}$). The final column measures the mass-dependent mass bias as the difference $\Delta b_{\log}^{\text{H-L}}$ between b_{\log} for the high- and low-mass clusters.

Hydrostatic mass	P	Q	$b_{\text{lin}}^{\text{cal}}$	b_{\log}	$b_{\log, \text{H}}$	$\Delta b_{\log}^{\text{H-L}}$
M_{500}^{CXC} , new Monte Carlo	1	0	0	$0.02^{+0.10}_{-0.08}$	$-0.09^{+0.11}_{-0.10}$	$-0.20^{+0.20}_{-0.16}$
M_{500}^{CXC} , incl. timestamp correction	0.946 ± 0.009	-0.002 ± 0.020	0.06 ± 0.00	$-0.01^{+0.10}_{-0.09}$	-0.11 ± 0.11	$-0.20^{+0.20}_{-0.16}$
M_{500}^{xmm} , full conversion	0.783 ± 0.007	0.062 ± 0.015	0.19 ± 0.01	$-0.08^{+0.10}_{-0.08}$	$-0.19^{+0.11}_{-0.10}$	$-0.21^{+0.20}_{-0.16}$
M_{500}^{xmm} , temperature effects only	0.799 ± 0.007	0.064 ± 0.015	0.17 ± 0.01	$-0.07^{+0.10}_{-0.08}$	$-0.18^{+0.11}_{-0.10}$	$-0.21^{+0.20}_{-0.16}$
M_{500}^{xmm} , no timestamp correction	0.826 ± 0.004	0.061 ± 0.007	0.15 ± 0.01	$-0.05^{+0.10}_{-0.08}$	$-0.16^{+0.11}_{-0.10}$	$-0.21^{+0.20}_{-0.16}$

For the eight clusters, we now find a pronounced bias of $b_{\log} = -0.08^{+0.10}_{-0.08}$, compared to $b_{\log} = 0.02^{+0.10}_{-0.08}$ from *Chandra*, using the updated Monte Carlo method. For the low-mass sub-sample, M_{500}^{xmm} and M_{500}^{wl} are consistent ($b_{\log} = 0.02^{+0.16}_{-0.12}$), while for the high-mass sub-sample, we measure $b_{\log} = -0.19^{+0.11}_{-0.10}$, i.e. M_{500}^{xmm} that are smaller than WL masses by a similar amount as the M^{pl} of vdL14 (cf. Fig. 3).

We repeat our analysis for a few modifications highlighting the relative importance of various contributing factors. First, we find that *Chandra* masses, converted to the newer CALDB v4.2 and the 0.7–7 keV band are systematically lower than for the V09a calibration and energy range. The *Chandra*-only timestamp calibration already accounts for ~ 30 per cent of the difference with *XMM-Newton*: $b_{\log} = -0.01^{+0.10}_{-0.09}$, a difference of $\Delta b_{\log} = -0.03$ (Table 1). This result is consistent with the higher masses the V09a pipeline returns in the Rozo et al. (2014a,b) cross-calibration studies. Conversely, omitting the timestamps correction moves up the M_{500}^{xmm} , such that $b_{\log} = -0.05^{+0.10}_{-0.08}$ is less negative by $\Delta b_{\log} = 0.03$. These comparisons demonstrate the importance of including the timestamp correction.

The 2 per cent difference the masses experience due to the different flux calibration of *Chandra* and *XMM-Newton* relates to a small, but measurable effect in the logarithmic bias. Ignoring it, we find a slightly milder bias of $b_{\log} = -0.07^{+0.10}_{-0.08}$ compared to the full conversion ($b_{\log} = -0.08^{+0.10}_{-0.08}$).

Considering the full mass range, the *XMM-Newton* hydrostatic masses are ~ 20 per cent lower than the WL masses, while *Chandra* masses are consistent with the WL masses. This indicates that if the $b_{\text{lin}} = 0.2$ linear hydrostatic bias in cluster simulations is correct, the effective area calibration of *XMM-Newton* is consistent with being correct. But if looking at the high-mass end, the conclusion is the opposite: *Chandra* is consistent with the correct calibration and 20 per cent hydro bias. The measurement uncertainties and the unknown amount of Eddington bias in our small sample, however, preclude more quantitative conclusions.

2.6 Mass-dependent bias with *XMM-Newton*

Finally, we measure the mass-dependence of the bias as the difference $\Delta b_{\log}^{\text{H-L}}$ between the logarithmic biases b_{\log} for the high- and low-mass clusters. This observable is stable against changes to the details of the probability distribution modelling in the Monte Carlo algorithm. [Note that fitting $\log(M^{\text{xmm}}/M^{\text{wl}})$ as a function of M^{wl} is not stable.]

In I14, the hydrostatic mass exhibited the least significant mass-dependent bias of four tested mass observables. For the four more massive clusters, b_{\log} is $\sim 1\sigma$ different to the four less massive

ones, as opposed to $\sim 2\sigma$. We reproduce this result and measure $\Delta b_{\log}^{\text{H-L}} = -0.20_{-0.16}^{+0.20}$ for *Chandra* and $\Delta b_{\log}^{\text{H-L}} = -0.21_{-0.16}^{+0.20}$ for *XMM-Newton* (Table 1).

We interpret the observed mass-dependence of b_{\log} as the superposition of (1) physical effects, e.g. the stronger hydrostatic bias for high-mass clusters Shi & Komatsu (2014) predict analytically, and (2) Eddington bias: as Sereno & Ettori (2014) demonstrate, intrinsic scatter in the abscissa mass leads to a mass-dependent bias when compared to an independent mass observable. Eddington bias is most severe in our case of a small sample size and a narrow range in the underlying true mass. In principle, the statistically complete nature of the 400d cosmology (V09a) sample would allow for a rigorous correction of such selection effects, once the WL follow-up has been completed. For our given sub-sample, the Eddington bias and true mass-dependent mass bias cannot be disentangled. While we can provide much needed *relative* cross-calibrations between X-ray and WL instruments/pipelines, selection effects preclude us from determining absolute calibrations for *Chandra* and *XMM-Newton*. Moreover, selection biases also limit the direct applicability of $\Delta b_{\log}^{\text{H-L}}$ to other cluster samples.

3 TRANSLATION TO PLANCK CLUSTERS

3.1 What did the Planck collaboration measure?

P13XX model the redshift-dependent abundance of clusters detected from the *Planck* catalogue of SZ sources (Planck Collaboration XXIX 2014, hereafter **P13XXIX**), covering the whole extragalactic sky. The thermal SZ effect describes the inverse Compton scattering of CMB photons with ICM electrons, resulting in a distortion Y_{SZ} of the CMB signal in the solid angle subtended by a galaxy cluster, proportional to the integrated electron pressure. All 189 S/N > 7 sources selected from the **P13XXIX** catalogue are confirmed clusters of known redshift; the vast majority with spectroscopic redshifts. The **P13XXIX** mass estimates M^{Pl} (M^{Yz} in **P13XXIX**) that enter the **P13XX** calculation are the only, and crucial, piece of *Planck* data **P13XX** used.

Due to the large beam compared to the typical *Planck* cluster size, the aperture size θ , in which Y_{SZ} is integrated, is hard to determine from the SZ data itself. **P13XXIX** rely on the additional $Y_{\text{SZ}}(\theta)$ constraint provided by the scaling of Y_{SZ} with an X-ray mass proxy, M_{500}^{Yx} , to fix θ and calibrate the M^{Pl} . By convention, r_{Δ} denotes a radius such that the mass M_{Δ} within it exceeds the critical density $\rho_c(z)$ at redshift z by a factor of Δ . The M_{500}^{Yx} mass proxy is based on $Y_{\text{X}} = T_{\text{X}} M_{\text{gas}}$, which is the product of the ICM temperature T_{X} and the cluster gas mass M_{gas} , measured from X-rays within r_{500} , and thus provides an X-ray analogue of Y_{SZ} .

P13XX calibrate M^{Pl} on a validation sub-sample of 71 clusters observed with *XMM-Newton*, i.e. they derive the best-fitting $Y_{\text{SZ}, 500} - M_{500}^{\text{Yx}}$ relation. In turn, M_{500}^{Yx} was calibrated on a sample of local, relaxed clusters whose ‘true’ masses could be measured using X-ray observations and assuming hydrostatic equilibrium (Arnaud et al. 2010). All EPIC instruments were used, with the pn/MOS normalization as a free parameter. Spectra were fitted in the 0.3–10 keV energy band (Arnaud, private communication). It is via this ladder of mass proxies that the hydrostatic mass bias is inherited on to M^{Pl} , appearing in the $Y_{\text{SZ}, 500} - M_{500}^{\text{Yx}}$ relation that summarises the calibration process (equation A.8 of **P13XX**). **P13XX** considered a flat prior of $0.7 < (1 - b_{\text{lin}}) < 1$, but any additional systematic effect in the calibration chain would mimic a spurious ‘hydrostatic’ bias.

3.2 Comparison to Planck and vdl14 samples

The mean WL mass of the **I14** high-mass sub-sample is $4.9 \times 10^{14} M_{\odot}$. The typical **P13XX** cluster mass, defined by their mass pivot $\sim 6 \times 10^{14} M_{\odot}$, falls into the mass range probed by the **I14** high- M^{wl} range, whether or not the mass bias is included. Therefore, for the relevant **P13XX** mass range, our result of $b_{\log, \text{H}} = 0.20_{-0.16}^{+0.17}$ agrees with the $1 - b_{\text{lin}} \approx 0.4$ that would reconcile cosmological constraints derived from *Planck* cluster counts (**P13XX**) and primary CMB anisotropies (**P13XVI**).

The high-mass end of the **I14** sample also overlaps with the **vdL14** sample. Using the M_{500}^{zmm} for the **I14** clusters instead of *Chandra* masses, we also find better agreement to the **vdL14** measurement of $\langle M^{\text{Pl}}/M^{\text{wl}} \rangle = 0.688 \pm 0.072$ for a subset of **P13XX** clusters. However, such comparisons are limited by the small number statistics of our sample, hence caution is necessary when interpreting these results.¹

Complications arise from the different energy range used for *Planck* and the temporal variability of X-ray calibrations. Our results for the cases with and without timestamp correction (Table 1) tell us, however, that the impact of those systematics is rather small, with $\Delta b_{\text{lin}} \lesssim 0.05$.

3.3 How much can X-ray calibration bias have influenced the P13XX results?

3.3.1 From Planck pre-calibration to calibration

We attempt to estimate how an additional bias $b_{\text{lin}}^{\text{cal}}$ arising from the *XMM-Newton* calibration relative to *Chandra* will influence the overall bias measured by **P13XX**. We emphasize that we do not know or assume which, if any, satellite calibration is correct. The ‘pre-calibration’ from 20 relaxed clusters (Arnaud et al. 2010) determines the normalization 10^{β} and slope β of a scaling relation

$$E^{-2/3}(z) \left[\frac{Y_{\text{X}}}{2 \times 10^{14} M_{\odot} \text{ keV}} \right] = 10^{\beta} \times \left[\frac{M_{500}^{\text{HE}}}{6 \times 10^{14} M_{\odot}} \right]^{\beta} \quad (6)$$

between the Y_{X} and hydrostatic masses M_{500}^{HE} measured with *XMM-Newton*. The evolution factor $E(z) = H(z)/H(z=0)$ depends on cosmology via the Hubble parameter $H(z)$.

In equation (6), M_{500}^{HE} scales roughly as $T_{\text{X}}^{3/2}$ (e.g. Kay et al. 2012), through the measurement at r_{500} . If $q = T_{\text{XMM}}/T_{\text{CXO}}$ for the typical Arnaud et al. (2010) cluster, hydrostatic masses are biased $M_{500}^{\text{HE}} \rightarrow q^{\delta} M_{500}^{\text{HE}}$, with $\delta \approx 1.5$. Similarly, Y_{X} depends on T_{X} via the measurement of the gas mass M_{gas} within r_{500} : we have $r_{500} \propto M_{500}^{1/3}$. If $M_{500} \propto T_{\text{X}}^{3/2}$ upon a change in T_{X} , then $r_{500} \propto (T_{\text{X}}^{3/2})^{1/3} = T_{\text{X}}^{1/2}$. Because $M_{\text{gas}}(< r)$ increases linearly with r in a given cluster,² it follows $M_{\text{gas}, 500} \propto T_{\text{X}}^{1/2}$ upon a change in T_{X} . Indeed, we measure $M_{\text{gas}, 500}$ to be affected as $q^{0.5-0.6}$ to by a relative temperature change q , using the **V09a** gas density model for the **I14** clusters. Hence, we

¹ The difference in cosmologies between **P13XX** and **vdL14** on the one hand (flat universe with matter density $\Omega_{\text{m}} = 0.3$ and Hubble parameter $H_0 = 70 \text{ km s}^{-1} \text{ Mpc}^{-1}$) and **I14** and this work the other hand (the same, but $H_0 = 72 \text{ km s}^{-1} \text{ Mpc}^{-1}$) adds a factor of 70/72 to convert *Planck* masses to our cosmology.

² If the cluster is isothermal, and $\rho_{\text{gas}} \propto r^{-2}$, as motivated by assuming the standard $\beta = 2/3$ in the β model for the gas density (Cavaliere & Fusco-Femiano 1978), then the 3D mass within a radius R is $M(< R) = \int_0^R \rho_{\text{gas}}(r) dV \propto \int_0^R r^{-2} r^2 dr = R$.

have $Y_X \rightarrow q^\gamma Y_X$ with an exponent $\gamma \approx 1.5$. Thus, T_X re-calibration affects equation (6) like

$$q^\gamma Y_X \propto [q^\delta M_{500}^{\text{HE}}]^\beta \Leftrightarrow Y_X \propto q^{\beta\delta - \gamma} [M_{500}^{\text{HE}}]^\beta. \quad (7)$$

For a (residual, unaccounted) temperature bias q , the mass proxy $M_{500}^{Y_X}$ will be biased by a factor $C = q^{\beta\delta - \gamma}$. This factor propagates into the main P13XX scaling relation, connecting the masses $M_{500}^{Y_X}$ to Y_{500} instead of Y_X :

$$E^{-2/3}(z) \left[\frac{D_A^2 Y_{\text{SZ},500}}{10^{-4} \text{Mpc}^2} \right] = 10^A q^{\alpha\delta - \gamma} \times \left[\frac{M_{500}^{Y_X}}{6 \times 10^{14} M_\odot} \right]^\alpha. \quad (8)$$

Here, D_A denotes the angular diameter distance. Because Y_X is theoretically expected to be proportional to Y_{SZ} , we identified $\alpha = \beta$ in equation (8).

3.3.2 Results for temperature re-calibration

The Arnaud et al. (2010) clusters used in the *Planck* pre-calibration show an average³ $k_B T_{\text{XMM}} \approx 5 \pm 2$ keV (Arnaud, Pointecouteau & Pratt 2007; Pratt et al. 2010). Following equation (3), the S14 conversion for the combined *XMM-Newton* instruments, *Chandra* temperatures for these clusters would be lower by a factor of $q = 0.84^{+0.05}_{-0.03}$.

Using $\alpha = 1.79 \pm 0.06$ from P13XX, and $\gamma = 1.5 \pm 0.3$ and $\delta = 1.5 \pm 0.3$ (i.e. allowing for broad uncertainties in both), we find the normalization of equation (8) to be reduced by a factor of $C = 0.81 \pm 0.09$.

3.3.3 Breaking the size–flux degeneracy

The exact algorithm by which P13XXIX combine *Planck* measurements with equation (8) has yet to be published. However, using $\theta_{500} = (3M_{500}/[4\pi\rho_c D_A^3])^{1/3}$, one can easily convert equation (8) into a scaling relation in terms of an aperture scale θ_{500} , i.e. $Y_{\text{SZ}} \propto \theta_{500}^{3\alpha}$. The intersection of this relation with the size–flux degeneracy modelled as $Y_{\text{SZ}}^{\text{obs}} \propto \theta^\lambda$ yields a point $(\theta_\times, Y_{\text{PI}})$, that can in turn be used to compute an SZ mass $M_{\text{PI}} \propto \theta_\times^3$. Thus, the degeneracy is broken. How is this M_{PI} affected if the normalization of equation (8) changes by a factor C ? We geometrically infer the changes in the intersection point and final mass as

$$\log(Y'_{\text{PI}}/Y_{\text{PI}}) = [-\lambda/(\lambda - 3\alpha)] \times \log C \quad (9)$$

$$\log C_{\text{fin}} = \log(M'_{\text{PI}}/M_{\text{PI}}) = [-3\alpha\lambda/(\lambda - 3\alpha)] \times \log C. \quad (10)$$

From Fig. 4 of P13XXIX, we read that the $Y_{\text{SZ}}^{\text{obs}} - \theta$ relation is linear, so $\lambda = 1$. With $C = 0.81^{+0.05}_{-0.03}$ from above, we find that cluster masses would be biased low by a factor $C_{\text{fin}} = 0.78^{+0.10}_{-0.07}$ due to the temperature calibration. Thus, if the *Chandra* calibration was correct, the need for a hydrostatic mass bias of more than the ~ 20 per cent favoured by simulations would be eased. Alternatively, if the *XMM-Newton* calibration was correct, evidence for stronger departures from hydrostatic equilibrium would persist.

We note that the ‘hydrostatic’ bias b_{lin} that P13XX consider is meant to include instrument calibration effects: $1 - b_{\text{lin}} = (1 - b_{\text{lin}}^{\text{hyd}})(1 - b_{\text{lin}}^{\text{xcal}}) \approx (1 - b_{\text{lin}}^{\text{hyd}} - b_{\text{lin}}^{\text{xcal}})$. Nevertheless, even a partially unaccounted calibration bias would contribute some of the apparent

³ In principle, the temperature re-calibration should be applied to individual clusters. This would alter the slope β in equation (6) in a similar way as the mass-dependent mass bias discussed below.

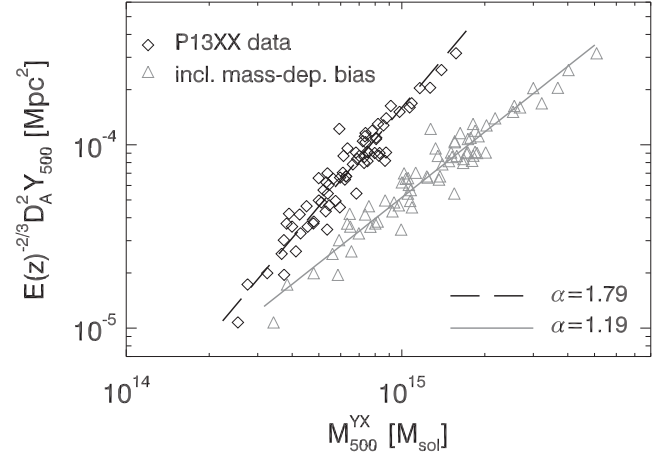


Figure 4. The P13XX calibration sample. Diamonds and the long-dashed fit line show the SZ signal as a function of original P13XX Y_X mass (compare their fig. A.1). Triangles and the solid fit line show re-scaled masses, assuming an extreme case of a mass-dependent hydrostatic bias.

mass discrepancy. The point of this exercise lies not in suggesting that the *Planck* discrepancy is caused by the X-ray calibration. Rather it should serve to demonstrate how such effects can not only fold through but even become amplified in a multistep calibration.

3.3.4 Inclusion of the mass-dependent bias

The above calculations treat the case of a potential residual temperature calibration offset in the *Planck* calibration. To this end, we assume the hydrostatic mass bias to be taken into account and well represented by the P13XX baseline value of $(1 - b_{\text{hyd}}) = 0.8^{+0.2}_{-0.1}$.

But it is instructive to include a mass-dependent hydrostatic mass bias, as suggested by I14 and Fig. 3. Because we are interested in extreme cases, we assume that the best-fitting $b_{\log}(M_{500}^{\text{xmm}}) = -0.346 \times (E(z)M_{500}^{\text{xmm}}/2.44 \times 10^{14} M_\odot) - 0.111$ is purely physical (departure from hydrostatic equilibrium). We emphasize that this is not the case. As detailed in Section 2.6, not all of the mass-dependence is physical, but an unknown fraction is caused by selection effects (Eddington bias).

Fig. 4 shows how a mass-dependent mass bias differentially stretches the mass range occupied by the *Planck* calibration clusters. In our extreme scenario, masses for all clusters are higher after accounting for b_{\log} (triangles) than before (diamonds), but most so for the most massive ones. Consequentially, the slope of equation (8) needs to be corrected from P13XX’s $\alpha = 1.79 \pm 0.06$ to a lower value of $\alpha = 1.19 \pm 0.04$.⁴

Interestingly, a flatter $Y-M$ slope largely cancels out the temperature re-calibration effect seen in Section 3.3.3. With $\alpha = 1.19 \pm 0.04$, we arrive at a factor of $C = 0.95^{+0.08}_{-0.05}$ in equation (8) and final *Planck* masses different by a factor of $C_{\text{fin}} = 0.94^{+0.11}_{-0.07}$. We conclude that inclusion of a mass-dependent hydrostatic bias that grows more negative with mass cannot increase the final calibration offset. The better, still partial, alleviation of the

⁴ Observations of the $Y-M$ relation have yet to reach an accuracy that would such constrain the mass-dependence of the hydrostatic bias. While Bender et al. (2014) and Czakon et al. (2014) report low best-fitting $Y-M$ slopes consistent with $\alpha \approx 1.2$, Liu et al. (2014) find a slope steeper than the self-similar value of $5/3$.

Planck cluster counts–CMB discrepancy is achieved from X-ray calibration effects alone.

4 SUMMARY

Starting from the recent S14 comparative study of ICM temperatures measured with *Chandra* and *XMM–Newton*, we revisit the bias between WL and hydrostatic masses from I14. We find the following.

(1) Because of different uncertainties in the effective area calibration, hydrostatic masses for the I14 clusters would have been measured to be ~ 15 – 20 per cent lower, had the clusters been observed with *XMM–Newton* instead of *Chandra*. The measured calibration bias depends on the sample, but can be transferred to clusters of similar mass (10^{14} – $10^{15} M_{\odot}$).

(2) *XMM–Newton* masses for the most massive I14 clusters are lower than WL masses by ~ 35 per cent.

(3) Assuming a true hydrostatic bias of $b_{\text{lin}}^{\text{hyd}} = 0.2$, our results for the whole mass range indicate that the calibration of the energy dependence of the effective area of the *XMM–Newton* EPIC instruments in the 0.6–10.0 keV band is rather accurate. In the high mass range, the data however indicate that *Chandra* calibration is more accurate. Given the uncertainties these results are not significant.

In addition, we consider the *Planck* clusters and find the following.

(4) Hence, consistent with vdL14, a bias of $(1 - b_{\text{lin}}^{\text{hyd}} - b_{\text{lin}}^{\text{xcal}}) \approx 0.4$ for the rather massive P13XX clusters seems plausible.

(5) If there was a residual calibration bias q in the T_{XMM} measurements on which the *Planck* analysis is based, the normalization of the P13XX $Y_{\text{SZ}} - M^{\text{Yx}}$ calibration would be affected as $C = q^{\sim 1.2}$. We show that the mass bias further amplifies when propagated into the SZ masses. Without accounting for calibration uncertainties, a mass bias of up to 20 per cent is plausible. We do not claim that this is the case for *Planck*. However, a small, residual bias would amplify in the same way. Pointing to the S14 result that calibration alone cannot explain the discrepant cosmological parameters of P13XVI and P13XXIX, we conclude that a possible contribution would ease the discrepancy and allow for a true hydrostatic bias consistent with simulations.

(6) A hydrostatic bias increasing with mass counteracts the amplification of a calibration bias.

Our results are consistent with the WL/X-ray mass biases recently reported by Donahue et al. (2014), comparing Cluster Lensing And Supernovae with Hubble (CLASH; Postman et al. 2012) WL mass profiles to those obtained with *Chandra* and *XMM–Newton*. Donahue et al. (2014) found their $T_{\text{XMM}}/T_{\text{CXO}}$ and $M^{\text{XMM}}/M^{\text{WL}}$ to depend on the integration radius, suggesting soft X-ray scattering as a cause for the calibration offset. Donahue et al. (2014) study mostly cool core clusters. Since S14 find that the T_{X} bias depends on T_{X} , this could explain why they find less bias in the cooler centres. The radial dependence could at least partly be due to a secondary correlation: at the radius where the cluster temperature is typically hottest, the largest discrepancy between *Chandra* and *XMM–Newton* is found.

Cluster mass calibrations still bear considerable uncertainties not only between the main techniques (X-ray, lensing, SZ, galaxy based), but also within techniques, i.e. for different instruments and calibration and methods. Thorough cross-calibration of different instruments and techniques, as already performed by Nevalainen et al. (2010), Rozo et al. (2014a,b) and Schellenberger et al. (2014)

for X-rays are the necessary way forward. Recent comparisons of WL masses to both *XMM–Newton* and *Chandra* include Mahdavi et al. (2013), Donahue et al. (2014), and Martino et al. (2014). We notice that Martino et al. (2014) find temperature discrepancies between *XMM–Newton* and *Chandra* similar to S14, but consistent hydrostatic masses from both satellites. More overlap between clusters with X-ray and WL data would be necessary to define mass standards against which other surveys could then be gauged.

Recently, Sereno & Etori (2014), Sereno, Etori & Moscardini (2014) compared several of the larger current WL and *XMM–Newton* and *Chandra* X-ray samples, emphasizing how intrinsic and measurement scatter can induce scaling relation biases. Sereno & Etori (2014) confirm that compared to simulated clusters WL masses are biased low by ~ 10 per cent and hydrostatic masses by ~ 20 – 30 per cent. However, these authors find literature masses from the same observable, X-ray or WL, can differ up to 40 per cent for the same cluster, impeding an absolute calibration. Sereno et al. (2014) extend the analysis to the *Planck* clusters, whose absolute mass calibration is likewise affected. They find scatter in the calibration scaling relation to invoke a mass-dependent bias in the *Planck* masses.

Here, the 400d cluster sample provides *relative* calibrations between the different instruments and methods. Once the WL follow-up has been completed, we will be able to disentangle the physical mass-dependent mass bias from selection effects and provide *absolute* calibrations.

The advent of larger SZ samples for scaling relation studies (e.g. Bender et al. 2014; Czakon et al. 2014; Liu et al. 2014), and foremost the all-sky P13XXIX offers the possibility of including a complementary probe and clusters at higher redshift. For future high-precision cluster experiments, e.g. *eROSITA* (Predehl et al. 2010; Merloni et al. 2012; Pillepich, Porciani & Reiprich 2012) or *Euclid* (Laureijs et al. 2011; Amendola et al. 2012), the absolute X-ray observable-mass calibration needs to be improved further.

ACKNOWLEDGEMENTS

We thank the *Planck* collaboration for making available the calibration sample in the SZ cluster data base (<http://szcluster-db.ias.u-psud.fr>). We thank the referee for helpful comments. HI would like to thank D. Applegate for a helpful discussion. HI acknowledges support from European Research Council grant MIRG-CT-208994 and Philip Leverhulme Prize PLP-2011-003. JN acknowledges a PUT 246 grant from Estonian Research Council. RJM is supported by a Royal Society University Research Fellowship. THR acknowledges support from the German Research Association (DFG) through Heisenberg grant RE 1462/5 and through the Transregional Collaborative Research Centre TRR33 ‘The Dark Universe’ (project B18). GS and THR acknowledge DFG grant RE 1462/6. This research has made use of the SZ-Cluster Database operated by the Integrated Data and Operation Center (IDOC) at the Institut d’Astrophysique Spatiale (IAS) under contract with CNES and CNRS.

REFERENCES

- Amendola L. et al., 2012, *Living Rev. Relativ.*, 16, 6
- Applegate D. E. et al., 2014, *MNRAS*, 439, 48
- Arnaut M., Pointecouteau E., Pratt G. W., 2007, *A&A*, 474, L37
- Arnaut M., Pratt G. W., Piffaretti R., Böhringer H., Croston J. H., Pointecouteau E., 2010, *A&A*, 517, A92
- Battye R. A., Moss A., 2014, *Phys. Rev. Lett.*, 112, 051303

- Bender A. N. et al., 2014, preprint ([arXiv:1404.7103](https://arxiv.org/abs/1404.7103))
- Bhattacharya S., Habib S., Heitmann K., Vikhlinin A., 2013, *ApJ*, 766, 32
- Burenin R. A., Vikhlinin A., Hornstrup A., Ebeling H., Quintana H., Mescheryakov A., 2007, *ApJS*, 172, 561
- Cavaliere A., Fusco-Femiano R., 1978, *A&A*, 70, 677
- Costanzi M., Sartoris B., Viel M., Borgani S., 2014, *J. Cosmol. Astropart. Phys.*, 10, 8
- Czakon N. G. et al., 2014, preprint ([arXiv:1406.2800](https://arxiv.org/abs/1406.2800))
- Donahue M. et al., 2014, *ApJ*, 794, 136
- Grant C. E., Guainazzi M., Natalucci L., Nevalainen J., Plucinsky P. P., Pollock A., Sembay S., 2013, preprint ([arXiv:1305.4480](https://arxiv.org/abs/1305.4480))
- Hamann J., Hasenkamp J., 2013, *J. Cosmology Astropart. Phys.*, 10, 44
- Israel H. et al., 2010, *A&A*, 520, A58
- Israel H., Erben T., Reiprich T. H., Vikhlinin A., Sarazin C. L., Schneider P., 2012, *A&A*, 546, A79 (I12)
- Israel H., Reiprich T. H., Erben T., Massey R. J., Sarazin C. L., Schneider P., Vikhlinin A., 2014, *A&A*, 564, A129 (I14)
- Kay S. T., Peel M. W., Short C. J., Thomas P. A., Young O. E., Battye R. A., Liddle A. R., Pearce F. R., 2012, *MNRAS*, 422, 1999
- Kelly P. L. et al., 2014, *MNRAS*, 439, 28
- Laganá T. F., de Souza R. S., Keller G. R., 2010, *A&A*, 510, A76
- Laureijs R. et al., 2011, preprint ([arXiv:1110.3193](https://arxiv.org/abs/1110.3193))
- Le Brun A. M. C., McCarthy I. G., Schaye J., Ponman T. J., 2014, *MNRAS*, 441, 1270
- Liu J. et al., 2014, preprint ([arXiv:1407.7520](https://arxiv.org/abs/1407.7520))
- Mahdavi A., Hoekstra H., Babul A., Bildfell C., Jeltama T., Henry J. P., 2013, *ApJ*, 767, 116
- Mantz A. B. et al., 2014, *MNRAS*, 446, 2205
- Martino R., Mazzotta P., Bourdin H., Smith G. P., Bartalucci I., Marrone D. P., Finoguenov A., Okabe N., 2014, *MNRAS*, 443, 2342
- Merloni A. et al., 2012, preprint ([arXiv:1209.3114](https://arxiv.org/abs/1209.3114))
- Nagai D., Kravtsov A. V., Vikhlinin A., 2007, *ApJ*, 668, 1
- Nevalainen J., David L., Guainazzi M., 2010, *A&A*, 523, A22
- Pillepich A., Porciani C., Reiprich T. H., 2012, *MNRAS*, 422, 44
- Planck Collaboration XVI, 2014, *A&A*, 571, A16 (P13XVI)
- Planck Collaboration XX, 2014, *A&A*, 571, A20 (P13XX)
- Planck Collaboration XXIX, 2014, *A&A*, 571, A29 (P13XXIX)
- Postman M. et al., 2012, *ApJS*, 199, 25
- Pratt G. W. et al., 2010, *A&A*, 511, A85
- Predehl P. et al., 2010, in Arnaud M., Murray S. S., Takahashi T., eds, *Proc. SPIE Conf. Ser. Vol. 7732, Space Telescopes and Instrumentation 2010: Ultraviolet to Gamma Ray*. SPIE, Bellingham, p. 77320U
- Rasia E. et al., 2012, *New J. Phys.*, 14, 055018
- Reese E. D., Kawahara H., Kitayama T., Ota N., Sasaki S., Suto Y., 2010, *ApJ*, 721, 653
- Reiprich T. H., Böhringer H., 2002, *ApJ*, 567, 716
- Reiprich T. H., Basu K., Etori S., Israel H., Lovisari L., Molendi S., Pointecouteau E., Roncarelli M., 2013, *Space Sci. Rev.*, 195
- Rozo E., Rykoff E. S., Bartlett J. G., Evrard A., 2014a, *MNRAS*, 438, 49
- Rozo E., Evrard A. E., Rykoff E. S., Bartlett J. G., 2014b, *MNRAS*, 438, 62
- Schaye J. et al., 2014, *MNRAS*, 446, 521
- Schellenberger G., Reiprich T. H., Lovisari L., Nevalainen J., David L., 2014, preprint ([arXiv:1404.7130](https://arxiv.org/abs/1404.7130)) (S14)
- Sereno M., Etori S., 2014, preprint ([arXiv:1407.7868](https://arxiv.org/abs/1407.7868))
- Sereno M., Etori S., Moscardini L., 2014, preprint ([arXiv:1407.7869](https://arxiv.org/abs/1407.7869))
- Shi X., Komatsu E., 2014, *MNRAS*, 442, 521
- Vikhlinin A., Markevitch M., Murray S. S., Jones C., Forman W., Van Speybroeck L., 2005, *ApJ*, 628, 655
- Vikhlinin A., Kravtsov A., Forman W., Jones C., Markevitch M., Murray S. S., Van Speybroeck L., 2006, *ApJ*, 640, 691
- Vikhlinin A. et al., 2009a, *ApJ*, 692, 1033 (V09a)
- Vikhlinin A. et al., 2009b, *ApJ*, 692, 1060 (V09b)
- von der Linden A. et al., 2014a, *MNRAS*, 439, 2
- von der Linden A. et al., 2014b, *MNRAS*, 443, 1973 (vdL14)

This paper has been typeset from a $\text{\TeX}/\text{\LaTeX}$ file prepared by the author.